Chapter 6

Decaying Kink Oscillations in the Fine-structured Cool Solar Jets

In this chapter, we perform a 2-D magnetohydrodynamic (MHD) simulations that provide a detailed picture of the evolution of cool jets caused by initial vertical velocity perturbations in the solar chromosphere. We implement random multiple velocity (V_{ij}) pulses of amplitude 20-50 km s^{-1} between 1.5 and 2.0 Mm in the solar atmosphere below the transition region (TR), which subject to the different switch-off periods between 50-300 s for the phase of the perturbations. These applied vertical velocity pulses create a series of magnetoacoustic shocks steepening above TR, and interacting with each other in the inner corona leading the complex localized velocity fields. The propagation of such perturbations create low-pressure regions behind and generate a variety of cool jets and associated plasma dynamics. We aim to study the oscillations of two cool jets J_1 and J_2 that move upto the height respectively 6.2 Mm and 5.4 Mm above TR. These jets are radially fine-structured in the density and Alfvén speed. The highly denser J_1, which is triggered along the significantly curved magnetic field lines, support

the propagation of the transverse kink waves of the period ≈195 s with a phase speed of ≈125 km s $^{-1}$. In the case of J_2, the evolved collective kink oscillations do not sustain for a longer time and dissipated quickly after one cycle. At the later stage, instead of collective oscillations of the jet, its outer surface possesses transverse oscillations locally without significantly perturbing the entire body of the jet. The different fine structures of the jets' spine oscillate locally in a transverse manner especially near the surface. We conjecture that the radial structuring of the density and characteristic Alfvén speed within J_1 and J_2, as well as the curvature of the magnetic field may generate leakage and dissipation of the wave-energy.

6.1 Introduction

The solar chromosphere and its intricate magnetic structures may generate numerous plasma ejecta such as solar jets, spicules, mottles, surges, magnetic swirls, network jets etc at diverse spatio-temporal scales. These plasma ejecta may contribute to input mass and energy into the upper layers of the Sun's atmosphere, i.e., transition region (TR) and corona. The movement/transfer of mass and energy from the lower atmosphere to the corona may be associated with various physical mechanisms contributing to the localized coronal heating, which is still an unsolved problem in the solar physics (e.g., De Pontieu et al., 2007b, 2014a, 2004; Hou et al., 2021; Jelínek et al., 2015; Kayshap et al., 2018; Liu et al., 2019; Mackenzie Dover et al., 2021; McIntosh et al., 2011; Panesar et al., 2020; Singh et al., 2022, 2019; Srivastava et al., 2020, 2017, 2018; Sterling, 2000; Sterling et al., 2010, and references cited therein). These chromospheric plasma ejecta are mostly collimated beam-like structures. These jets are associated with a variety of magnetohydrodynamic (MHD) waves, oscillations, and instabilities. The observations from space-borne and ground based instruments reveal that these jet-like structures are critical to understand a

range of physical processes that occur in the solar atmosphere (e.g., shocks, instabilities, heating, waves, flux-emergence and reconnection). The extensive studies reveal that such structures are ubiquitous and quasi-periodic on the limb and disk in the solar atmosphere. These jet-like structures are categorized based on their physical properties (e.g., De Pontieu et al., 2007b, 2014a; Jelínek et al., 2015; Mackenzie Dover et al., 2021; McIntosh et al., 2011; Samanta et al., 2019; Singh et al., 2022, 2019; Srivastava et al., 2018; Tian et al., 2014, and references cited therein).

Recent high-resolution observations reveal that the chromospheric jet and jet-like structures (e.g. network jets, magnetic swirls, network-jet, spicule-like rotating plasma structures, etc) are triggered quasi-periodically reaching at various heights (2-12 Mm) in the solar atmosphere. The typical life time of these jets is 3-12 min and their maximum velocity is found between 10-150 km s^{-1} (e.g., De Pontieu et al., 2007b, 2014a; Pasachoff et al., 2009, and references cited therein). These jets are cool ($\simeq 10^4$ K) and thin structures (300-1100 km), which disappear in the chromospheric lines before their downfall (e.g., Pasachoff et al., 2009). This effect may be caused by the jet's cool material is rapidly expanding or getting hot by some heating mechanism therein (Takasao et al., 2013). Therefore, the evolution of such cool jets and associated plasma processes provide a deep insight about their triggering mechanisms in the solar atmosphere. Various single and two-fluid MHD models provide the detailed picture behind the evolution and triggering mechanism of these jets as well as the physics of associated various drivers in the lower solar atmosphere. These models primarily generate perturbations in the form of gas pressure and velocity pulses that interact with the magnetized plasma. These interactions and complex structuring of magnetic field may also allow the magnetic reconnection at small spatial scales, which cause the localized heating and the formation of jet-like plasma ejecta in the lower solar atmosphere (e.g., De Pontieu et al., 2004; González-Avilés et al., 2021; Heggland et al., 2007; Hou et al., 2021; Iijima and Yokoyama, 2017; Jelínek et al.,

2015; Kayshap et al., 2013b, 2018; Kuźma et al., 2017b; Murawski and Zaqarashvili, 2010; Murawski et al., 2011; Nishizuka et al., 2008; Shibata et al., 1992a; Singh et al., 2019; Yokoyama and Shibata, 1995, and references cited therein).

Several extensive observations reveal that the inhomogeneous and complex motion of the plasma produce various modes of the oscillations and instabilities in the jets. These modes of oscillations and instabilities generated *in-situ* either by very complex plasma motions near the region of the concentration of field lines or by the shearing motions in the ambient plasma of the jet's spire. Hence, these oscillations and instabilities dramatically extend the view of the jets. The jet like structures may oscillate along the field lines with 5 min period (e.g., De Pontieu et al., 2003; Kulidzanishvili and Zhugzhda, 1983; Xia et al., 2005; Zaqarashvili and Erdélyi, 2009). The oscillations across the axis of the jet have been reported by Kukhianidze et al. (2006) and Jess et al. (2011). These transversal oscillations show the periodic behaviour due to generation of the kink waves. The propagation of the kink waves in the jet-like structures can be traced using the spectral observations of $H\alpha$ (e.g., Jess et al., 2011). However, there are several controversy in the interpretation of transverse oscillations in the jet like structures. It may be Alfvén waves, or kink waves or Alfvénic waves (e.g., De Pontieu et al., 2003; Jess et al., 2011; Zaqarashvili and Erdélyi, 2009). The MHD waves which have the wave number equal to one (i.e., m=1) are called kink oscillations while Alfvénic waves are described as a signature of predominantly a mixed mode in the in-homogeneous waveguides (Srivastava et al., 2021a). The linear kink waves are incompressible in nature which exhibit the periodic displacement resulting from the magnetic tension force (e.g., Goossens et al., 2009). These transverse kink oscillations are ubiquitous in the jet-like structures, and they have been found mainly due to the overshooting of complex and shearing motion of the plasma as a rebound shock and convective motion of the photospheric plasma (e.g., Sterling and Hollweg, 1988; Vranjes et al., 2008). It is well known that lower solar atmospheric oscillations are susceptible

to the features of mode coupling, in which one magnetoacoustic wave mode is coupled to the another one (slow or fast magnetoacoustic waves), and the wave energy can be transferred to another mode in certain particular atmospheric conditions (e.g., Nakariakov and Verwichte, 2005). Apart from this, the kink oscillations are ubiquitously detected in a variety of coronal and chromospheric structures, and their dissipation is mostly governed by exclusive plasma processes (e.g., resonant absorption), which are set-in due to the transverse inhomogeneities of the plasma (e.g., density), magnetic field, and characteristic velocities across the flux tube (e.g., Goossens et al., 2002, 2006; Nakariakov et al., 2021; Srivastava et al., 2021a).

In this chapter, we provide a description of the evolution of various fine-structured cool jets under the influence of the random vertical velocity perturbations in the chromosphere creating a complex velocity field. The especial emphasis is further given on the study of two cool jets possessing the decaying kink oscillations. We perform a 2D numerical simulations of the non-linear MHD equations for a single fluid plasma with the implementation of vertical velocity pulses around the null point configuration of the magnetic field. The transverse oscillating jets in our model remind the peculiar observational signature of the kink oscillations in the cool jet-like structure as reported in various previous literature (e.g., Jess et al., 2011). We analyse the triggering mechanism of kink oscillations, their properties, and most likely reason of their dissipation in these model jets. The chapter is structured as follows. Section 6.2 provides the description of basic MHD model of the solar atmosphere and the initial equilibrium configuration. Section 6.3 describe the numerical methods. In section 6.4, we describe the velocity perturbations. Section 6.5 presents the simulation results. Section 6.6 outlines the discussion and conclusions.

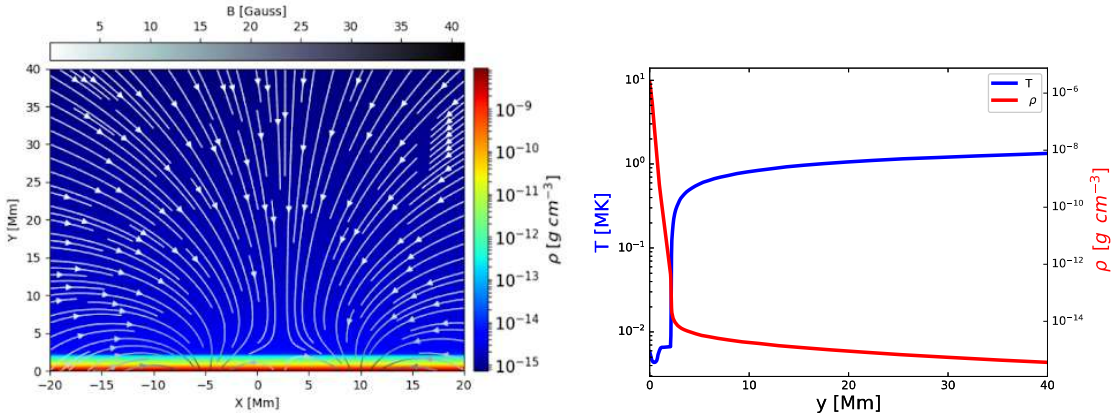

Figure 6.1: Left: The equilibrium magnetic field lines in the stratified model solar atmosphere. The null point formed above the TR in lower corona. Right: The variation of temperature (T) (blue-curve) and mass density (ρ)(red curve) w.r.t. vertical direction (y) in the model solar atmosphere.

6.2 Numerical Model of the Generation of Oscillating Spicule-like Cool Jets

We consider an ideal MHD system (see Eqs. 2.4-2.9 in Chapter 2, without adding cooling effects of radiation and thermal conduction terms in Eq. 2.8) which is used to model and study the triggering of various plasma ejecta and waves present in the gravitationally stratified and magnetized solar atmosphere. In this model, we do not consider non-ideal effects such as dissipative effects, resistivity, magnetic diffusivity, heating and/or cooling effects of the plasma, and also avoid the initial velocity of the plasma particles. In the present chapter, we develop the MHD model to understand the evolution of various cool jets on both sides of a magnetic null point geometry.

Initially, there is no plasma movement in the considered model of the solar atmosphere (i.e., $V_e = 0$). Therefore, it implemented from the photosphere to the inner corona (i.e., 40 Mm) in its static equilibrium. This model atmosphere is supported by force-free and also current-free medium. Therefore, the configuration of magnetic field is initially expressed as (e.g., Singh et al., 2022, 2019; Srivastava et al., 2020)

$$\nabla \times \mathbf{B} = \mathbf{0}, \qquad (\nabla \times \mathbf{B}) \times \mathbf{B} = \mathbf{0}. \tag{6.1}$$

The equilibrium configuration of the magnetic field **B** with the null point geometry is estimated as (e.g., Low, 1985):

$$B_x = \frac{-2S_1(x-a_1)(y-a_2)}{((x-a_1)^2+(y-a_2)^2)^2} + \frac{-2S_2(x-b_1)(y-b_2)}{((x-b_1)^2+(y-b_2)^2)^2} + \frac{-2S_3(x-c_1)(y-c_2)}{((x-c_1)^2+(y-c_2)^2)^2} + \frac{-2S_4(x-d_1)(y-d_2)}{((x-d_1)^2+(y-d_2)^2)^2}, \tag{6.2}$$

$$B_y = \frac{2S_1(x-a_1)^2 - S_1((x-a_1)^2+(y-a_2)^2)}{((x-a_1)^2+(y-a_2)^2)^2} + \frac{2S_2(x-b_1)^2 - S_2((x-b_1)^2+(y-b_2)^2)}{((x-b_1)^2+(y-b_2)^2)^2} + \frac{2S_3(x-c_1)^2 - S_3((x-c_1)^2+(y-c_2)^2)}{((x-c_1)^2+(y-c_2)^2)^2} + \frac{2S_4(x-d_1)^2 - S_4((x-d_1)^2+(y-d_2)^2)}{((x-d_1)^2+(y-d_2)^2)^2}, \tag{6.3}$$

$$B_z = 0. \tag{6.4}$$

Here, B_x and B_y represent the magnetic field components in the horizontal (i.e., X-axis) and vertical (i.e., Y-axis) directions respectively. There is no magnetic field in the transverse direction i.e., $B_z = 0$. The symbols S_1, S_2, S_3 and S_4 represent the strength of the magnetic poles. We take them as $S_1 = S_3$ = -56 Gauss while $S_2 = S_4$ = 1120 Gauss, which create the resultant null point configuration of the magnetic field in the model solar atmosphere (Fig 6.1, left-panel). The pair of the notations [a_1, a_2], [b_1, b_2], [c_1, c_2] and [d_1, d_2] depicts the positions of the magnetic poles S_1, S_2, S_3 and S_4, respectively. Here, we specify the notations a_1, b_1, c_1 and d_1 as the positions of the corresponding pole on horizontal spatial span (i.e., X-axis), while a_2, b_2, c_2 and d_2 are the positions of the corresponding pole on a vertical spatial span (i.e., Y-axis). We fix the horizontal positions of the poles as a_1 = -10.0 Mm, b_1 = -5.0 Mm, c_1 = 5.0 Mm and d_1 = 10.0 Mm on the

X-axis. We also fix the vertical positions of the poles as $a_2 = c_2$ = -10.0 Mm, $b_2 = d_2$ = -5.0 Mm below the photosphere boundary (i.e., 0.0 Mm). Therefore, the resultant magnetic field lines originate from the convection zone. The null point geometry of the magnetic field lines is shown at the middle of the field of view in inner corona (above TR; see Fig. 6.1). The field lines on both of its sides are curved fields that smoothly extend up to 40 Mm in the vertical direction as visualized in the model solar atmosphere (see Fig. 6.1, left-panel). Some of the low-lying loop structures are also evident filling the lower corona and chromosphere as usual. The lower bottom limit of the model solar atmosphere is fixed at 0.0 Mm, which represents the bottom of the solar photosphere. We launch the pulses above the solar photosphere, so there are no dynamics occurring below the photosphere boundary. We took the position and strength of the magnetic fields of the poles in such a way that we could fix the location of the null point in the model solar atmosphere.

We consider a realistic and gravitationally stratified model solar atmosphere that initially follows the hydrostatic equilibrium condition. This states that the force arising from pressure gradient is equal to the force arising from the acceleration due to gravity. Therefore, both forces are balanced and makes the medium force-free. The expression for this is as follows (e.g., Singh et al., 2022, 2019; Srivastava et al., 2020):

$$-\nabla p + \rho \mathbf{g} = 0. \tag{6.5}$$

We express the equilibrium configuration of the mass density and thermal pressure in the model solar atmosphere, which initially maintains the hydrostatic equilibrium. The thermal pressure and mass density w.r.t. vertical direction (y) are determined as (e.g., Singh et al., 2022, 2019; Srivastava et al., 2020)

$$p_e(y) = p_{ref} exp\left(-\int_{y_{ref}}^{y} \frac{dy'}{\Lambda(y')}\right), \tag{6.6}$$

and

$$\rho_e(y) = \frac{p_e(y)}{g\Lambda(y)}, where, \Lambda(y) = \frac{k_B T_e(y)}{\hat{m}g}. \tag{6.7}$$

Here, p_{ref} denotes the thermal pressure at the reference level y_{ref}=10 Mm. The subscript 'e' indicates that the associated variables are in equilibrium.

We consider the magnetized and gravitationally stratified solar atmosphere, in which all background physical parameters are structured vertically. The temperature (T_y) variation w.r.t vertical direction (y) in the realistic model solar atmosphere is illustrated in Fig. 6.1 (right blue curve). This temperature profile was calculated by analyzing observed line profiles in the solar atmosphere by Avrett and Loeser (2008). The typical value at height y=0.0 Mm in this temperature profile is ≃5807 K, which corresponds to the Sun's photospheric temperature. As one ascends higher in altitude, the typical value gradually decreases to ≃4350 K at altitude y=0.5 Mm. This temperature value represents at the top photosphere/bottom chromospheric temperature. In the present temperature profile, the solar transition region is located at altitude y≃2.1 Mm, where the temperature rises sharply and reaches ≃100931 K. The equilibrium profile of mass density w.r.t. height (y) is shown in the Fig. 6.1 (red-curve). This profile is expressed by the above equations (Eqs. 6.6 & 6.7). The value of mass density at y=0.0 Mm (i.e. the solar photosphere) of the order of 10^{-6} gcm^{-3}, while at y=0.5 Mm (the solar chromosphere), it attains the order of 10^{-8} gcm^{-3}. We notice that on moving towards the higher altitudes, the values of the mass density smoothly falls. At the transition region, i.e., y=2.2 Mm in our model atmosphere, the value of the mass density falls by 10^{-8} times of the photospheric mass density.

6.3 Numerical Methods

We use the PLUTO code to solve the single fluid ideal MHD equations (Eqs. 2.4-2.9, without adding cooling effects of radiation and thermal conduction terms in Eq. 2.8)

numerically (e.g., Mignone et al., 2007b). It solves the set of non-linear MHD equations by implementing the initial and boundary conditions. The initial setup for the model solar atmosphere is chosen to be responsible for the generation of the cool jets from the chromosphere along the magnetic field lines. Our model assume to be invariant along the z-direction (i.e., $\partial/\partial \mathrm{z} = 0$) and with fixed $B_z = V_z = 0$ throughout the simulation. In this modelling, the time integration is calculated using the third order Runge-Kutta (RK3) method (cf. Chapter 2, Section 2.4.7). We apply the Roe solver to solve the flux calculation using decomposition of the Roe matrix (cf., Chapter 2, Section 2.4.6) of the characteristics (cf., Mignone et al., 2007b). We also apply the Courant-Friedrichs-Lewy number to 0.25, which sounds a quite small. The details of the numerical setup is described by e.g., Singh et al. (2019), Srivastava et al. (2020), and Singh et al. (2022).

We fixed the model solar atmosphere with a horizontal span (x) of 40 Mm (-20 Mm, 20 Mm) and a vertical span (y) of 40 Mm (0 Mm, 40 Mm). In this 2-D space, we implement the static grid to set the spatial resolution. In this model, the horizontal span is equally divided by 2560 cells as uniform grid. We cover the vertical span by using uniform and stretched grids both, equally divided by 320 cells from 0.0 to 5.0 Mm and 1120 cells from 5.0 to 40 Mm. Therefore, the spatial resolution is 15.625 km per numerical cell for the uniform grid and 31.25 km per numerical cell for the stretched grid in our model solar atmosphere. We fix the stretched grids from 5.0 Mm and above in the simulation box. The vertical velocity signals produced by the perturbations are very weak at the top zone in the simulation box. Therefore, the incoming signal is diffused near the top zone boundary due to the presence of the stretched grids set in that particular region of the simulation box. The incoming signals have no discernible effect on the jet triggering during the transition from uniform grids to the stretched grids. Therefore, the non-linearity of the grid distribution save the computation time of the numerical code. In our model, we apply the min-mod limiter, which works well for a diffusion aspect by reducing/restricting the reflection of the

signal from the overlying region (top-zone) of the simulation domain (e.g., Singh et al., 2022). However, there is no substantial dynamics occurred in the top zone of the simulation box, which would have an effect on the region of interest, located around the transition region of our model solar atmosphere. The null point is located just above the transition region and magnetoacoustic shocks are produced. This triggered the field aligned cool plasma in form of solar jets from the chromosphere. We run the simulation with the eight processors using multiple passage interface (MPI) up to 1800 s and save the output data file on every 5 s.

We apply all four boundaries of the simulation domain which ensure that the boundary maintains the equilibrium values of all the plasma quantities. We established user-defined boundaries which is the simplest approach for having pretty well-working boundaries in the presence of gravity in our stratified model solar atmosphere. The details of the imposed boundary conditions are described in various literatures (e.g., Singh et al., 2022, 2019; Srivastava et al., 2020). The details of PLUTO code structure and numerical methods are given in Chapter 2.

6.4 Perturbations

Initially, we applied 30 randomly generated vertical velocity pulses in the chromosphere between 1.0-1.5 Mm height, which are responsible for the generation of cool jets along the magnetic field lines in the model solar atmosphere. Theses vertical velocity perturbations are applied for a fixed time range from 50 to 300 s (e.g., Mackenzie Dover et al., 2021). The applied perturbations are expressed as follows (e.g., Mackenzie Dover et al., 2021):

$$V_y = A_v \times exp\left(-\frac{(x-x_0)^2+(y-y_0)^2}{w^2}\right) \times \left[tanh\left(\frac{\pi(t-P)}{P}+\pi\right)+1.0\right], \tag{6.8}$$

Here, A_v depicts the amplitude of the velocity pulse, while the pair 'x_0' and 'y_0' represent the horizontal (x) and vertical (y) positions of the pulse. The symbol 'w' depicts the full width at half maximum (FWHM) of the applied Gaussian pulse. The symbol 't' depicts time and 'p' represents the period of the pulse. In the present model, we applied 30 random vertical velocity pulses of the amplitudes ranging between 20-50 kms^{-1}. We chose the value of w ranging between 50-100 km. These pulses have been applied between -10 and 10 Mm on the horizontal axis and between 1.0 and 1.5 Mm on the vertical axis. The above expression of the Gaussian pulse with a hyperbolic tangent, which is used to switch-off the velocity perturbation after certain cutoff period. We select the period (P) of the pulses ranging between 50 and 300 s (e.g., Mackenzie Dover et al., 2021). These strong vertical velocity pulses generate a variety of cool jets in which two jets exhibit the transverse (kink) oscillation (cf., Fig. 6.2).

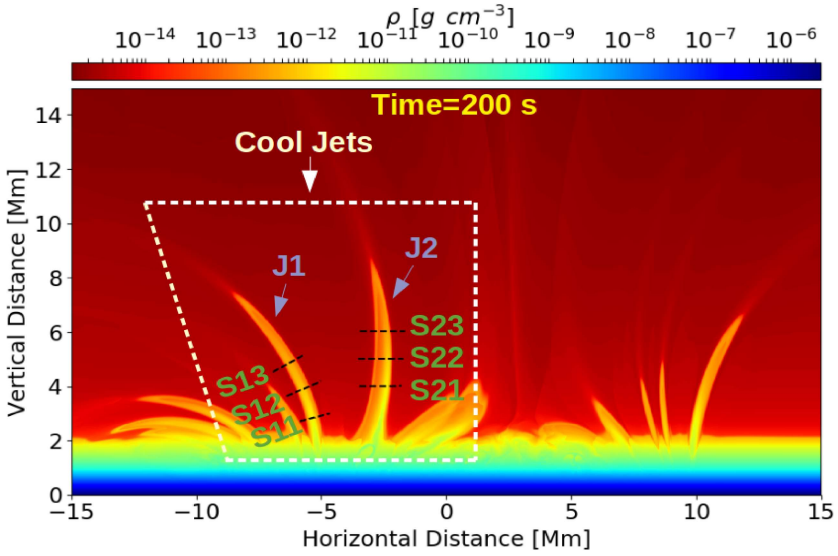

Figure 6.2: The mass density (ρ) profile with six dotted slits chosen on the cool jets J_1 and J_2', where we estimate the distance–time diagrams over these chosen slits. The FoV demonstrates the evolution of various cool jets and plasma flows.

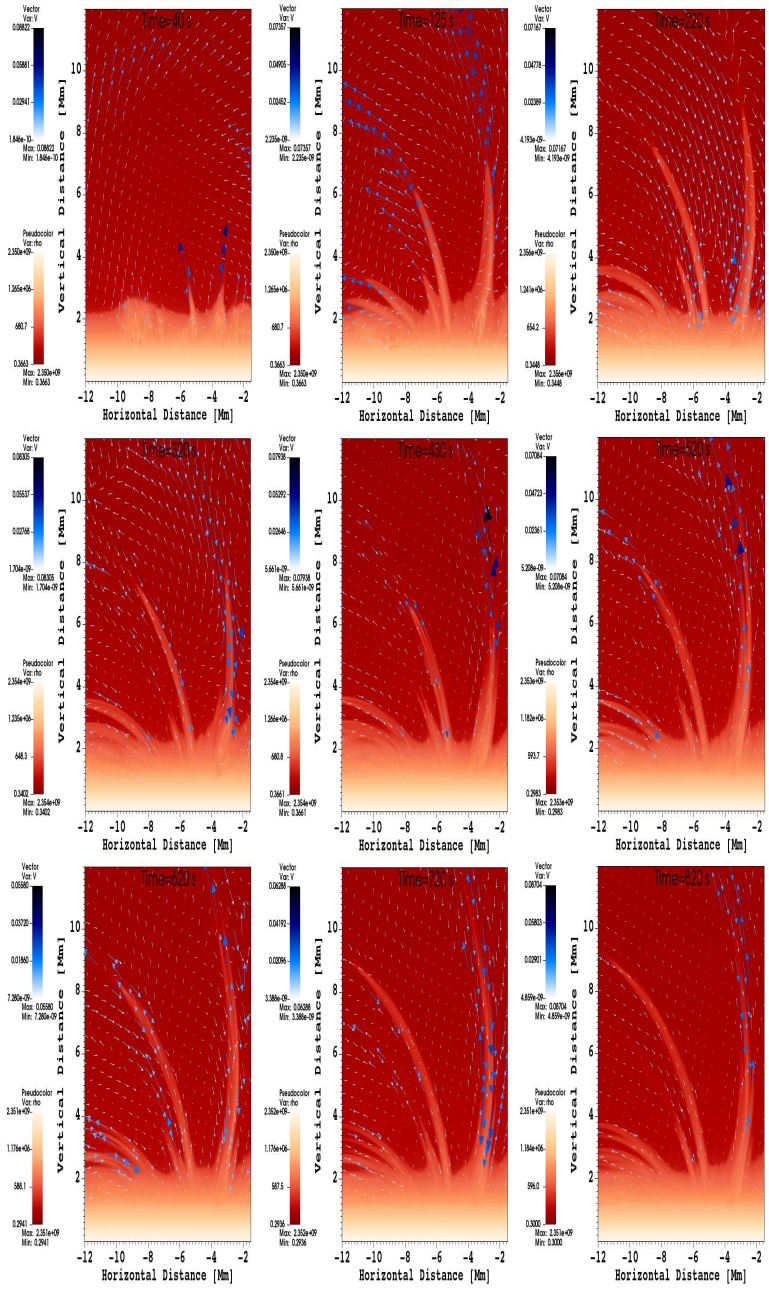

Figure 6.3: The normalized density map of the evolution of cool jets. The jet J_1 and J_2 as highlighted in Fig. 6.2. These cool jets are triggered by the implementation of random vertical velocity (V_y) pulses initially. The pulses are applied in the chromosphere between 1.0 and 1.5 Mm. The normalized velocity vectors are over-plotted on each density map between t = 0 and 820 s.

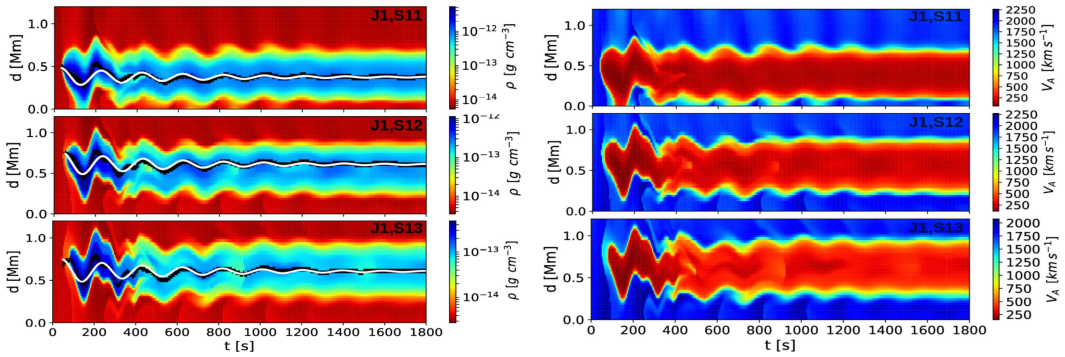

Figure 6.4: Left: The distance-time diagrams in density for the jet 'J_1' corresponding to the slits S11, S12 and S13 in Fig. 6.2. These diagrams show the decaying kink waves in the jet 'J_1'. They also display the radial structuring of the density across the oscillating jet. Right: The distance-time diagrams in Alfvén velocity for jet 'J_1' corresponding to the slits S11, S12 and S13 as shown in Fig. 6.2. These maps clearly demonstrate the radial structuring of the Alfvén speed across the oscillating jet.

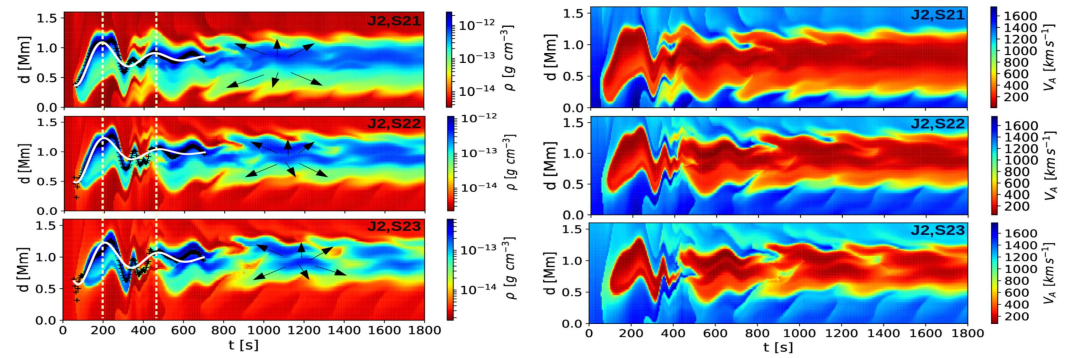

Figure 6.5: Left: The distance-time diagrams in density for jet 'J_2' corresponding to the slits S21, S22 and S23 as shown in Fig. 6.2. These diagrams show the decaying kink oscillations in jet 'J2', which quickly seized in one cycle. These diagrams also display the radial structuring of the density across the oscillating jet. Right: The distance-time diagrams in Alfvén velocity for jet the 'J_2' corresponding to the slits S21, S22 and S23 as shown in Fig. 6.2. These maps clearly demonstrate the radial structuring of the Alfvén speed across the oscillating jet.

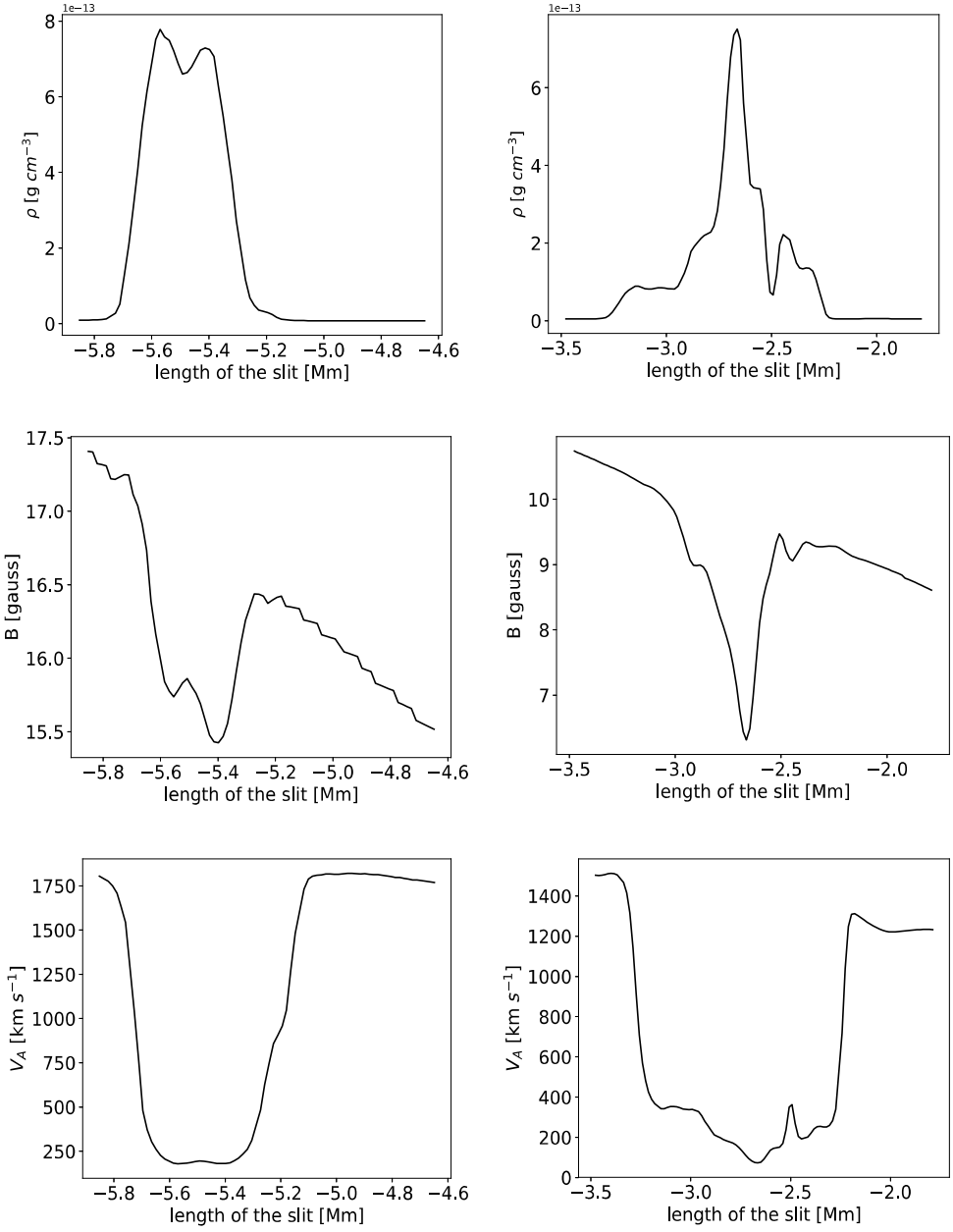

Figure 6.6: Top row represents the density vs length, middle row the magnetic field vs length, and bottom row the Alfvén speed vs length of the slits S11 (for Jet J_1) (right column) and S21 (for jet J_2) (left column) at t=800 s. This clearly demonstrates that when we move radially outward the density decreases while the magnetic field and Alfvén speed increase.

6.5 Evolution of the Transverse Kink Waves in the Cool Jets

The random vertical velocity pulses triggered in the solar chromosphere, further create a series of field-aligned magnetoacoustic perturbations in the solar atmosphere. The magnetized solar atmosphere is possessing a typical magnetic structuring with a null point Eventually, if there is only one such pulse, it will indeed generate a slow magnetoacoustic shock while moving up into the stratified solar atmosphere. This will also create a low pressure region which further enable the movement of the cool plasma upward forming a cool spicule-like jet (Murawski and Zaqarashvili, 2010; Murawski et al., 2011).

In a similar manner, when multiple such pulses propagate initially from the solar chromosphere to the transition region and thereafter in the inner corona, they steepen in form of multiple field-aligned shocks and cause the evolution of a variety of cool jets as shown in Fig. 6.2. These spicule-like cool jets rise and fall quasi-periodically as recently reported by Singh et al. (2022). In this chapter, we focus on the dynamics of two spicule-like cool jets J_1 and J_2 as displayed in Fig. 6.2 within a box made by dotted-white line. The details of the plasma dynamics at the null-point is out-of-scope of this chapter.

These two jets are evolved along the curved magnetic field lines (cf., Figs. 6.2-6.3). These jets rise-up to the height of 6.2 Mm and 5.4 Mm respectively above the solar transition region (TR). The fine-structured plasma (with different density streaks) flow along the curved field lines forming the spine of these two jets (cf., Fig. 6.3). The multiple magnetoaocustic shocks interact with each other and with the null-point region in the inner corona that further create a localized complex velocity field in and around the evolved jets. Moreover, the jet's spine becomes fine-structured, with its core at higher density while the outer periphery maintained at lesser density as evident in Fig. 6.2 & 6.6.

The evolved spicule-like cool jets J_1 and J_2 came into the influence of the complex velocity fields, which are locally created in the inner corona above the TR. This further triggers the transverse oscillations into these jets. This oscillation bends the axis of the jet as a whole, thus termed as transverse kink waves. To analyze the physical properties of the evolved transverse oscillations, we select slits S11, S12, S13 at jet J_1, and slit S21, S22, S23 at jet J_2 (cf., Fig. 6.2). The derived distance-time diagrams in density (left panel) and Alfvén velocity (right panel) for J_1 are shown in Fig. 6.4. On the similar manner, the derived distance-time diagrams in density (left panel) and Alfvén velocity (right panel) for J_2 are shown in Fig. 6.5.

Table 6.1: Fitting parameters of the kink oscillations in jets (J_1 and J_2)

Jet	Slit	Amplitude (Mm)	Beta (s^{-1})	Omega (rad s^{-1})	Phi (rad)
J_1	S11	$0.1143^{+0.0067}_{-0.0067}$	$0.0018^{+0.0001}_{-0.0001}$	$0.0318^{+0.0001}_{-0.0001}$	$-0.95857^{+0.0582}_{-0.0582}$
	S12	$0.1557^{+0.0099}_{-0.0099}$	$0.0018^{+0.0001}_{-0.0001}$	$0.0323^{+0.0001}_{-0.0001}$	$-1.3568^{+0.0596}_{-0.0596}$
	S13	$0.1545^{+0.0117}_{-0.0113}$	$0.0018^{+0.0002}_{-0.0002}$	$0.0325^{+0.0002}_{-0.0002}$	$-1.4839^{+0.0729}_{-0.0729}$
J_2	S21	$0.6111^{+0.0429}_{-0.0429}$	$0.0044^{+0.0004}_{-0.0004}$	$0.0238^{+0.0005}_{-0.0005}$	$1.5708^{+0.0004}_{-0.0004}$
	S22	$0.7158^{+0.0581}_{-0.0581}$	$0.0053^{+0.0005}_{-0.0005}$	$0.0226^{+0.0007}_{-0.0007}$	$1.5708^{+0.0054}_{-0.0054}$
	S23	$0.6343^{+0.0651}_{-0.0651}$	$0.0043^{+0.0005}_{-0.0005}$	$0.0222^{+0.0007}_{-0.0007}$	$1.5708^{+0.0288}_{-0.0288}$

Fig. 6.4 shows the decaying kink oscillations. The fitted decaying sinusoidal curve confirms the evolution of decaying kink waves in the first jet. The fitting function is given as follows:

$$y(t) = b + A\exp(-\beta t)\cos(\omega t + \phi) \tag{6.9}$$

Where, the symbol 'b' describes the background, 'A' represents the amplitude, 'β' the damping coefficient in s^{-1}, 'ω' the frequency of oscillation in radian s^{-1}, and 'ϕ' tells about the phase shift in radian.

The kink oscillations at three different heights along jet J_1 are shown in top (for slit S11), middle (for slit S12) and bottom (for slit S13) panels in Fig. 6.4 (left) in the density. The fitting parameters of these oscillations are given in Table 6.1. The amplitude of the oscillations lies in the range of ≈114-155 km s^{-1}, while the damping time is ≈550 s and wave-period is ≈195 s. The highly denser J_1, which triggered along the significantly curved magnetic field lines, supports the propagating transverse kink waves of the period ≈195 s at a phase speed of ≈100 km s^{-1}. The propagation speed is derived by estimating the distance between slit S11 and S13, which is ≈2 Mm, and the phase difference estimated as ≈0.52 radian (cf., Table 6.2). The relation between the phase difference, period 195 s (or frequency 'f'), and time-delay is $\nabla\phi = 360^0 \times f \times \nabla t$. The phase difference of 0.52 radian gives almost 29.79^o, and period 195 s estimates the frequency as 5.12 mHz. The time-delay between the wave propagation between slit S11 and S13 is estimated approximately as 16 s. Therefore, the phase speed of kink wave in the high density jet is estimated as 125 km s^{-1}. The wavelength of the propagating kink wave is estimated as large as ≈24000 km. By assuming, a straight and slender flux tube, the kink speed c_k can also be expressed as (Nakariakov and Verwichte, 2005)

$$c_k = \sqrt{\frac{\rho_i C_{Ai}^2 + \rho_e C_{Ae}^2}{\rho_i + \rho_e}} \tag{6.10}$$

where $\rho_i, \rho_e, C_{Ai}, C_{Ae}$ are respectively the internal and external densities and Alfvén speeds. In the core of J_1, the Alfvén speed is around ≈125 km $^{-1}$, while just outside it is around ≈ 500 km s^{-1} (cf., right panel of Fig. 6.4). Similarly, the density contrast ρ_e/ρ_i is almost 0.01 (cf., left panel of Fig. 6.4). Therefore, the estimated kink speed c_k is found to be ≈128 km

s^{-1}. The speed derived from the fitting parameters of the kink oscillations (Table 6.1) and time-lag analyses is consistent with the one derived by the mean of MHD theory.

The strongly decaying kink oscillations are also evolved in the second jet. In the case of J_2, the evolved collective kink oscillations do not sustain longer beyond its one cycle (cf., Fig. 6.5), and dissipate quickly. At the later stage, instead of collective oscillations of the spine of J_2, its outer surface possesses the transverse oscillations without significantly perturbing the inner core. The kink oscillations are not decaying very rapidly for the first 1000 s in the case of J_1, however, after this time-span, they decay from the jet's spine in next 800 s, and this jet is being relaxed. In the case of J_2, the damping is strong with the time-scale of ≈188-227 s. Its strong oscillation amplitude (600-700 km) quickly seized after one cycle of the kink oscillations. The one important feature is noticed in J_2 that after 800 s, the different fine structures of the jet spine oscillate locally in a transverse manner especially near the surface.

We conjecture that the radial structuring of the density and characteristic Alfvén speed within J_1 and J_2, as well as the curvature of the magnetic field cause onset of the leakage of the wave-energy outward to dissipate these kink waves in these jets. The kink oscillation decays smoothly in J_1 at each heights (S11-S23).

6.6 Discussion and Conclusions

The jets J_1 and J_2 are propelled up into the inner corona carrying the cool and denser plasma. They are also subjected to the kink oscillations. Over the given time, these jets are also subjected to the fine-structured plasma flows along their spine. This creates a radial variation of density, magnetic field, and Alfvén speeds in both the jets. Moreover, they are formed on the spine of the curved magnetic field lines. Top row of Fig. 6.6 represents the density vs length, middle row the magnetic field vs length, and bottom row the Alfvén speed vs length along the slits S11 (right column) and S21 (left column) at

t=800 s respectively for J_1 and J_2 jets. This describes that when we move radially outward in the jet the density decreases while the magnetic field and Alfvén speed increase.

In the highly denser jet J_1, which is triggered along the significantly curved magnetic field lines, the propagating transverse kink waves of period 195 s at a speed of 125 km s^{-1} is evolved. In the case of second jet (J_2), the evolved collective kink oscillations no longer sustain beyond its one cycle, and dissipate quickly. The dissipation of kink waves can also occur due to the wave leakage by the curved magnetic field of the jets (e.g., Aschwanden 2004, 2014), as well as the radial homogeneity generated across the jet.

In the next Chapter 7, we discuss the evolution of Kelvin-Helmholtz (K-H) instability as seen in the cool plasma component of a coronal jet in the solar atmosphere.